Numerical estimation of the permeability of granular soils using the DEM and LBM or FFT-based fluid computation method

Ngoc-Son Nguyen, François Bignonnet

Noname manuscript No.
(will be inserted by the editor)

Numerical estimation of the permeability of granular soils using the DEM and LBM or FFT-based fluid computation method

Ngoc Son Nguyen · François Bignonnet

the date of receipt and acceptance should be inserted later

Abstract Numerical packings of spheres with uniform grain size distribution and maximum to minimum diameter ratio up to 15 are generated using the Discrete Element Method (DEM). Two numerical methods are used to compute their permeability by homogenization: the Lattice Boltzmann Method (LBM) and a Fast Fourier Transform (FFT) based method. The results given by both methods are shown to be consistent with semi-analytical and experimental results. For an identical discretization grid, the FFT method has the lowest memory and computational time requirements. The LBM is more accurate for coarse to moderately fine discretizations, while the FFT method converges linearly with the voxel size h with a relative discretization error below 1.5 times h/D_{25}, where D_{25} is the 25% passing by mass grain diameter. The issue of the variability of the permeability computed on finite sized samples is determined either directly by many realizations of similar random samples or indirectly by a faster filtering method on a single sample. Both methods yield similar results and indicate that a Representative Volume Element (RVE) size greater than $7D_{40}$ guarantees a variability of permeability below 5%.

Keywords Granular materials · Permeability · Discrete Element Method (DEM) · Lattice Boltzmann method (LBM) · Fast Fourier Transform (FFT) · Homogenization

1 Introduction

Granular soils have been widely used to construct hydraulic earth-filled structures such as dams, dikes and levees. The permeability K is a key parameter used in the Darcy law to describe the fluid flow in such media. An accurate

E-mail: ngocson-nguyen@univ-nantes.fr · E-mail: francois.bignonnet@univ-nantes.fr
Nantes Université, École Centrale Nantes, CNRS, GeM, UMR 6183, F-44600 Saint-Nazaire, France

estimation of this parameter is of paramount importance to assess the safety of hydraulic earth-filled structures. In fact, these structures might suffer from several instabilities caused by the seepage, among them internal erosion is one of the main causes of failures of embankment dams and dikes [17]. Internal erosion is a phenomenon during which fine particles migrate through the pore space between coarse particles under the action of seepage forces. This migration of fine particles leads to a degradation of hydraulic and mechanical properties of the soil, which might result in damages or failures of earth-filled structures. Therefore, the risk assessment requires an accurate prediction of the flow velocity and pore pressure inside the structure, and then accurate permeability values of the soils that constitute the structure. The permeability can be determined by performing tests in-situ or in laboratory. However, these tests are costly and time-consuming. Moreover, due to the soil's heterogeneity in terms of grain size distribution (GSD) and compactness, an important number of tests is needed to obtain a reliable assessment, leading to a high cost. Empirical relations have been extensively used as an alternative to estimate the permeability of granular soils from their GSD and porosity. Most of empirical relations link the permeability to D_{10} (grain diameter corresponds to 10 % finer by mass) considered as the characteristic grain diameter and porosity (see [35] for different empirical formulas). Each relation has been developed for a specific class of materials with a specific range of GSDs. An inappropriate use of these empirical rules might lead to an underestimation or overestimation of the permeability by several orders of magnitude as stated by Koltermann and Gorelick [27] and Odong [35]. Kenney et al. [25] found that the permeability of a granular filter is closely related to its controlling constriction size D_c^* which is the diameter of the largest particle that can be transported through the void space of the filter. This is the starting point for the semi-empirical method proposed by Indraratna et al. [23] who estimated the controlling constriction size D_c^* by using a probabilistic method based on the GSD.

As the geometry of the void space of the granular soil is determinant of the permeability, a reliable method for estimating this parameter should take the microstructure into account. Nowadays, the power of the computer and advanced technologies allow us to extract the microstructure of real porous materials by using micro-computed tomographic scans (micro-CT) or to simulate realistic virtual materials. The DEM (discrete element method) has been widely used to model granular soils at the particle scale from their GSD and density [36]. Other numerical soil models include the sequential deposition algorithm [13]. The microstructure extracted from simulated samples serves as input to compute the permeability by using a numerical fluid computation method. Different methods can be used to solve fluid flow through the void space, among them finite-difference method [15], lattice Boltzmann method (LBM) [18,28,39] and FFT-based (Fast Fourier Transform) upscaling method [7,9,32] are grid-based methods. These methods present a great interest as the uniform grid used to discretize a porous medium is convenient not only for virtual materials simulated using DEM but also for real materials whose mi-

crostructure is digitized into a series of images with high resolution. For example, the permeability and conductivity of random beds of particles constructed by the sequential deposition algorithm has been thoroughly investigated by [13,33] using the finite-difference method. Other methods such as Immersed Boundary Method (IBM) used by Knight et al. [26] and Semi-Implicit Method of Pressure Linked Equations (SIMPLE) method used by Sanvitale et al. [38] can also be applied to uniform grids. Nevertheless, mesh refinements at the particle surface are required to improve the accuracy of the numerical solution.

In this paper, we use the LBM and FFT-based upscaling method to compute the permeability of granular materials simulated with the DEM. Our first objective is to compare these two methods in terms of their accuracy and performance. For this comparison, we use some benchmark problems for which precise solutions can be obtained by semi-analytical approaches or by computations with very high resolution. We also validate numerical results given by these two methods against experimental data available in literature for glass beads. Our second objective is to provide some guidelines when choosing the resolution of the discretized microstructure and the size of the Representative Volume Element (RVE). The RVE size must be chosen to obtain a reliable permeability from random finite sized samples generated with the DEM. For this purpose, the direct method proposed by Kanit et al. [24] is first used to estimate the variance of the permeability for a given RVE size from many realizations and compared against a faster filtering method from a single realization presented in [1,7]. Both methods are compared on series of numerical results obtained with the DEM combined with the FFT-based upscaling method.

This paper is organized as follows. We first recall briefly the framework for upscaling permeability from fluid flow simulations at the pore scale. We then present the DEM used to simulate granular samples considered in this study and the LBM and FFT-based upscaling method to compute the permeability. Next, the accuracy and performance of the LBM and FFT-based upscaling method are compared by using some benchmark problems. Finally, we present a study on the discretization resolution and the RVE size to compute the permeability from DEM generated samples.

2 Upscaling of Darcy's law from Stokes equations

We consider the description of flow of an incompressible Newtonian fluid of dynamic viscosity μ through a porous medium[1]. The flow is assumed sufficiently slow to neglect inertia effects.

[1] $\mu = \rho\nu$ where ρ is the fluid density and ν its kinematic viscosity.

At the macroscopic scale, Darcy's law linearly relates the filtration velocity $\boldsymbol{V}$ to the macroscopic pressure gradient ∇P via the permeability tensor $\boldsymbol{K}$:

$$\begin{aligned} &\nabla \cdot \boldsymbol{V} = 0 \\ &\boldsymbol{V} = -\frac{\boldsymbol{K}}{\mu} \cdot \nabla P \end{aligned} \tag{1}$$

At the microscopic scale, the flow within the pore space is instead governed by Stokes equations. Within the framework of periodic homogenization [2,3,16], a homogenization problem P_{Stokes} is defined on a Representative Volume Element (RVE) Ω comprising a fluid phase Ω_{f}, a rigid solid phase Ω_{s} and a solid-fluid interface Γ. The size of the RVE must be much smaller than the characteristic length of fluctuation of the fields at the macroscopic scale to ensure the description by a continuum at the macroscopic scale, but it must be much larger than the characteristic length of the pore space to ensure the representativity of the RVE. As a result, the macroscopic velocity $\boldsymbol{V}$ and pressure gradient $\boldsymbol{F} = \nabla P$ from (1) appear as constants within the RVE. At the pore scale, the fluid velocity $\boldsymbol{v}$, the pressure and the Cauchy stress tensor are fields of the microscopic space variable $\boldsymbol{x}$. The pressure p_{tot} (resp. Cauchy stress $\boldsymbol{\sigma}_{\text{tot}}$) in the fluid decomposes in a linear trend due to the macroscopic pressure gradient $\boldsymbol{F} = \nabla P$ and a periodic fluctuation p (resp. $\boldsymbol{\sigma}$) as:

$$p_{\text{tot}} = \boldsymbol{F} \cdot \boldsymbol{x} + p \qquad ; \qquad \boldsymbol{\sigma}_{\text{tot}} = -(\boldsymbol{F} \cdot \boldsymbol{x})\mathbf{1} + \boldsymbol{\sigma} \tag{2}$$

where $\mathbf{1}$ is the identity second order tensor. For the periodic fluctuation variables, the flow appears driven by $\boldsymbol{F}$:

$$\begin{aligned} &\nabla \cdot \boldsymbol{\sigma} - \boldsymbol{F} = 0 && \text{in } \Omega_{\text{f}} \\ &\boldsymbol{\sigma} = -p\mathbf{1} + 2\mu\nabla^s \boldsymbol{v} && \text{in } \Omega_{\text{f}} \\ &\nabla \cdot \boldsymbol{v} = 0 && \text{in } \Omega_{\text{f}} \\ &\boldsymbol{v} = \mathbf{0} && \text{on } \Gamma \\ &\boldsymbol{v} \text{ and } p \text{ periodic} && \text{on } \partial\Omega \end{aligned} \tag{3}$$

where $\nabla^s \boldsymbol{v}$ is the symmetric part of the microscopic velocity gradient.

By linearity of problem (3), the solution velocity field $\boldsymbol{v}$ linearly depends on the macroscopic pressure gradient $\boldsymbol{F}$ via some velocity concentration tensor field $\boldsymbol{\kappa}$ such that:

$$\forall \boldsymbol{x} \in \Omega, \quad \boldsymbol{v}(\boldsymbol{x}) = -\frac{1}{\mu}\boldsymbol{\kappa}(\boldsymbol{x}) \cdot \boldsymbol{F} \tag{4}$$

where, by extension, $\boldsymbol{v}$ is set to $\mathbf{0}$ in Ω_s. The macroscopic velocity $\boldsymbol{V}$ is related to its microscopic counterpart by the averaging rule:

$$\boldsymbol{V} = \overline{\boldsymbol{v}}^{\Omega} \quad \text{with} \quad \overline{\boldsymbol{v}}^{\Omega} = \frac{1}{|\Omega|}\int_{\Omega} \boldsymbol{v}\, \mathrm{d}V \tag{5}$$

The combination of (4) and (5) shows that the macroscopic velocity $\boldsymbol{V}$ is linearly related to the macroscopic pressure gradient $\boldsymbol{F}$ by the permeability tensor $\boldsymbol{K}$ of the porous medium used in (1), defined as:

$$\boldsymbol{K} = \overline{\boldsymbol{\kappa}}^{\Omega} \tag{6}$$

In numerical homogenization, the homogenization problem (3) is solved for prescribed values of the macroscopic pressure gradient $\boldsymbol{F}$ corresponding to the base vectors $\boldsymbol{e}_j$, $j \in \{1, 2, 3\}$. The components v_i of the computed velocity fields then directly correspond to components κ_{ij} of the velocity concentration tensor; averaging over the RVE provides the upscaled permeability according to (6).

3 DEM generated samples and LBM and FFT-based upscaling methods

3.1 DEM generated granular samples and grid-based discretization

Granular samples having periodic boundary conditions are simulated by using the DEM implemented in the open-source software YADE [44]. These samples are composed of spherical particles whose diameters match a given GSD. The interactions between particles at the contact are described by two linear force-displacement laws in the normal and tangential interactions. The tangential interaction must respect Coulomb friction law. The parameters needed for numerical simulations are the same as those used in [40]: particle mass density $\rho = 2600$ kg/m^3, particle normal stiffness $k_n/D = 250$ MPa (D is the particle diameter), particle tangential stiffness $k_t/k_n = 0.5$, and the friction angle $\varphi = 35°$. The value of k_n chosen here is high enough to obtain inter-particle overlaps δ/D smaller than 0.5%. Particles are first generated into a cubic box in such a way that the sample's boundaries are periodic. The box sizes are chosen such that the particles do not greatly overlap each other. The box sizes are then progressively reduced until either the sample's porosity or the stresses reach target values.

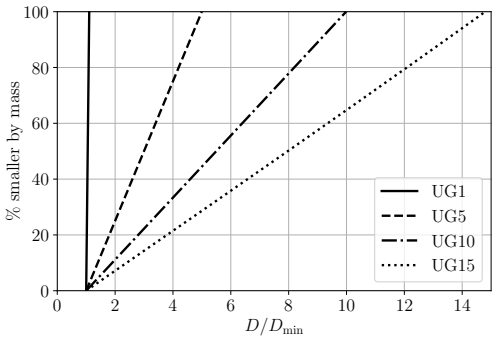

Fig. 1 Four grain size distributions (GSDs) considered in the current study: UG1, UG5, UG10, UG15.

Four different types of granular samples, namely UG1, UG5, UG10 and UG15, composed of spherical particles with linearly graded GSDs are simu-

lated (Figure 1). The last number of each label designates the value of the maximum to minimum particle diameter ratio $D_{\max}/D_{\min}$. For instance, the samples UG15 have $D_{\max}/D_{\min} = 15$. The samples UG1 are actually almost monosized where the particle diameter D varies narrowly between $0.95\overline{D}$ and $1.05\overline{D}$ with $\overline{D}$ being the average particle diameter. These samples are models of actual samples of monosized glass beads tested by Verneuil and Durian [42]. The three other types of samples UG5, UG10 and UG15 are categorized as uniformly graded materials. The porosity is controlled to be equal to 0.38 for all the samples. The hydraulic radius R_H defined as the ratio of the total pore volume V_p to the total pore surface S_p ($R_H = V_p/S_p$) is computed for each sample. According to Carman-Kozeny equation [12], the permeability of granular materials is mainly controlled by the hydraulic radius R_H and the porosity. Table 1 shows the coefficient of uniformity C_u, the porosity and the hydraulic radius R_H of the simulated samples.

Sample	UG1	UG5	UG10	UG15
C_u	1.05	2.4	3.4	3.9
porosity	0.38	0.38	0.38	0.38
$R_H/D_{\min}$	0.1	0.25	0.39	0.52

Table 1 Coefficient of uniformity C_u, porosity and hydraulic radius R_H of the four types of samples.

A uniform grid is used to discretize a granular sample into nodes and cells as illustrated in Figure 2. This discretization allows us to describe the microstructure of the sample, and it serves as input to the LBM and FFT-based upscaling method to compute the permeability. The former operates on the nodes, while the latter operates on the cells, otherwise called pixels in 2D or voxels in 3D. The length of the sides of each cell is denoted by h. A node is considered as a solid one if it is located inside a solid particle and as a fluid one otherwise (Figure 2.b). Among the solid nodes, those having at least one neighboring fluid node are considered as the nodes at the fluid-solid interface. In a quite similar way, a cell is considered as a solid one if its center is located inside a solid particle; furthermore, the solid cells having at least one neighboring fluid cell are considered as those at the fluid-solid interface (Figure 2.c).

3.2 LBM

A fluid can be viewed as either a collection of distinct molecules at the microscale or a continuum at the macroscale[2]. At the microscale, the dynamics of each molecule can be modeled by the molecular dynamics (MD). However,

[2] In this section, as opposed to Section 2, the microscale denotes the molecular scale, the macroscale denotes the scale at which the fluid is homogeneous (which is the microscale of Section 2) and the mesoscale denotes the scale of a collection of molecules.

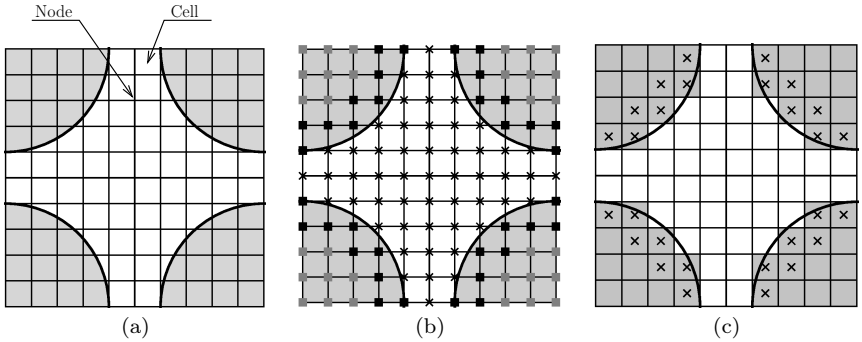

Fig. 2 2D illustration of the discretization using a uniform grid. (a) solid particles (gray) and fluid (white). (b) solid nodes (■ for the bulk nodes and ■ for the nodes at the interface) and fluid nodes (×), and (c) solid cells (gray cells and those with × depict the cells at the interface) and fluid cells (white cells).

this method is extremely expensive as a huge number of particles is required to represent the fluid. Most CFD (computation fluid dynamics) methods such as FEM (finite element method) or FVM (finite volume method) use a macroscopic description of the fluid by means of the well-known Navier-Stokes equation. This equation describes the motion of the fluid in terms of macroscopic variables such as flow velocity and pressure, similarly to (3) (in which inertia effects are neglected). The LBM adopts a mesoscopic view of the fluid and lies between the aforementioned methods. According to this method, the fluid is viewed as a set of different populations of molecules; in each population, all the molecules move in the same direction and at the same velocity. Each population is described by a distribution function $f(\boldsymbol{x}, \boldsymbol{\xi}, t)$ which represents the proportion of the molecules having a microscopic velocity $\boldsymbol{\xi}$ at position $\boldsymbol{x}$ and time t. The macroscopic variables such as the fluid density $\rho(\boldsymbol{x}, t)$ and flow velocity $\boldsymbol{v}(\boldsymbol{x}, t)$ are related to the distribution function $f(\boldsymbol{x}, \boldsymbol{\xi}, t)$ and the microscopic velocity $\boldsymbol{\xi}$ by integrals over the microscopic velocity space. The evolution of the distribution function $f(\boldsymbol{x}, \boldsymbol{\xi}, t)$ is described by the Boltzmann equation associated with the BGK collision model [5]. This equation is numerically solved by discretizing the whole fluid domain into a regular lattice with a spacing h and the continuous velocity space $\boldsymbol{\xi}$ into a set of discrete velocities $\boldsymbol{\xi}_i$ ($i = 0, 1, ..., N$). We use the model D2Q9 with 9 discrete velocities and D3Q19 with 19 discrete velocities for 2D and 3D problems, respectively. The discretized forms of the Boltzmann equation associated with the BGK collision model are as follows:

$$\rho(\boldsymbol{x}, t) = m \sum_{i=0}^{N} f_i(\boldsymbol{x}, t), \quad \rho(\boldsymbol{x}, t)\boldsymbol{v}(\boldsymbol{x}, t) = m \sum_{i=0}^{N} \boldsymbol{\xi}_i f_i(\boldsymbol{x}, t) \tag{7}$$

$$f_i(\boldsymbol{x} + \boldsymbol{\xi}_i \Delta t, t + \Delta t) = f_i(\boldsymbol{x}, t) - \frac{\Delta t}{\lambda}[f_i(\boldsymbol{x}, t) - f_i^{\mathrm{eq}}(\boldsymbol{x}, t)], \tag{8}$$

where f_i depicts the distribution function at a given node along direction i; m is the molecule mass which is usually taken as being a unit for simplicity; Δt is the time step; λ is a relaxation time; and $f_i^{\text{eq}}(\boldsymbol{x}, t)$ is the so-called *equilibrium* distribution function and is obtained by truncating the Hermite expansion of the Maxwell-Boltzmann distribution to the 2nd order:

$$f_i^{\text{eq}} = \omega_i \rho \Big[1 + \frac{3(\boldsymbol{\xi}_i.\boldsymbol{v})}{c_s^2} + \frac{9(\boldsymbol{\xi}_i.\boldsymbol{v})^2}{2c_s^4} - \frac{3(\boldsymbol{v}.\boldsymbol{v})}{2c_s^2}\Big], \tag{9}$$

where c_s is referred to as the sound speed, and coefficients ω_i depend on the discretization model [21]. For instance, for the D3Q19 model, $c_s = (h/\Delta t)/\sqrt{3}$, $\omega_0 = 1/3$, $\omega_{1,..,6} = 1/18$ and $\omega_{7,..,18} = 1/36$. For a flow with low Match number $M = \mid \boldsymbol{v} \mid /c_s$ ($M \ll 1$), the Navier-Stokes equation can be recovered from the discrete Boltzmann equation (8) combined with (7) and (9) by using the multiscale Chapman-Enskog analysis [20]. Through this multiscale analysis, the pressure p and fluid kinematic viscosity ν are related to the density ρ and the relaxation time λ, respectively, as follows:

$$p = c_s^2 \rho \tag{10}$$

$$\nu = \Delta t c_s^2 \Big(\tau - \frac{1}{2}\Big), \tag{11}$$

where $\tau = \lambda/\Delta t$ is the dimensionless relaxation time. Equation (11) requires that $\tau > 1/2$.

The system of equations (7) and (8) is numerically solved by simply repeating a collision step followed by a streaming step. For the collision step, all the populations at a given node $\boldsymbol{x}$ and at a given time t collide each other, and the post-collision distribution function $f_i^c(\boldsymbol{x}, t)$ for each population is computed as:

$$f_i^c(\boldsymbol{x}, t) = f_i(\boldsymbol{x}, t) - \frac{1}{\tau}[f_i(\boldsymbol{x}, t) - f_i^{\text{eq}}(\boldsymbol{x}, t)], \tag{12}$$

where the equilibrium distribution function f_i^{eq} is given by (9) with the macroscopic density ρ and velocity $\boldsymbol{v}$ given by (7). After that, each population is streamed to the neighboring node in its direction after the time period Δt:

$$f_i(\boldsymbol{x} + \boldsymbol{\xi}_i \Delta t, t + \Delta t) = f_i^c(\boldsymbol{x}, t). \tag{13}$$

The above collision and streaming steps are only applied on the fluid nodes. The no-slip boundary condition at the fluid-solid interface is accounted for by the so-called *full way bounce-back scheme*. Due to the presence of the solid phase, some pre-collision distribution functions at the fluid nodes near the interface are unknown as no population is streamed from the solid nodes. These unknown distributions at time t (those are represented by dotted arrows in Figure 3.d) are determined by making the following assumption. For the post-collision populations that are streamed from a fluid node into a solid node at the interface at time $t - 2\Delta t$ (f_4^c, f_7^c and f_8^c in Figure 3.a), they arrive at the solid node at time $t - \Delta t$ (Figure 3.b), then reverse their direction (Figure

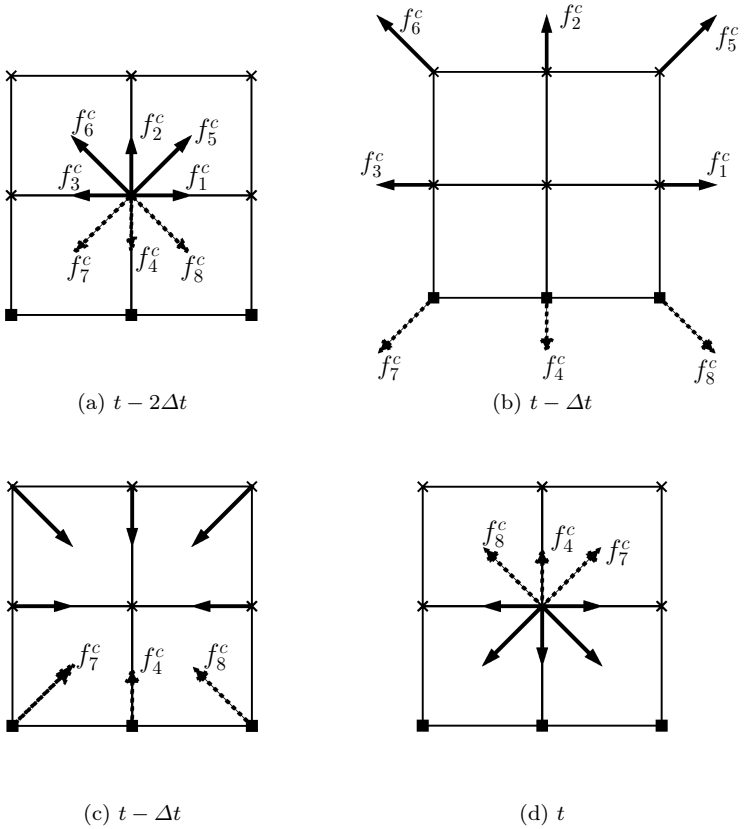

(a) $t - 2\Delta t$ (b) $t - \Delta t$

(c) $t - \Delta t$ (d) t

Fig. 3 Illustration of the full way bounce-back scheme for the populations between fluid nodes ($\times$) and solid nodes ■.

3.c) and finally come back to its original fluid node at time t (Figure 3.d). Therefore, the unknown pre-collision distribution functions at the fluid node at time t (f_2, f_5 and f_6) are the known post-collision distribution functions in the respective opposite directions at the same node but at time $t - 2\Delta t$ (f_4^c, f_7^c and f_8^c, respectively). It follows that

$$f_i(\boldsymbol{x}, t) = f_{-i}^c(\boldsymbol{x}, t - 2\Delta t), \tag{14}$$

where f_i is an unknown pre-collision distribution function and f_{-i}^c is the post-collision distribution function in the opposite direction. It should be noted that only populations f_4^c, f_7^c and f_8^c in Figure 3.c reverse their direction, the other populations are streamed from the neighboring fluid nodes. The above full way bounce-back scheme is used to impose the no-slip velocity at the fluid-solid interface; nevertheless, it has a low accuracy. Indeed, for the Poiseuille flow for which the solid nodes are located on the walls, it was found that the slip velocity is not zero at the walls and is of first order in space ($O(h)$)

[22]. The slip velocity is actually zero at halfway between the fluid and solid nodes. Some other bounce-back schemes have been proposed to improve the accuracy such as the scheme of Bouzidi et al. [10] for which some ghost nodes are added on the fluid-solid interface where the bounce-back takes place. This scheme can be used when the solid phase has simple geometries. For instance, this scheme was used in [41] for 2D fluid flow between circular particles. For complex geometries of the solid particles, it is difficult to use this scheme and the computation is not efficient. In our study, we use the full way bounce-back scheme owning to its computational efficiency and to the fact that the precise location of the fluid-solid interface is not known in our discretization method presented in Section 3.1.

For the outer boundaries, the periodic boundary conditions are used in the three directions. In this case, all the populations that leave a given fluid node will enter the corresponding fluid node on the opposite side. The pressure gradient $\boldsymbol{F} = \nabla P$ is imposed at each fluid node as a body force, similarly to (3). In the LBM, taking into consideration the body force is not straightforward and can be indirectly done by modifying the collision operator (12) and the equilibrium distribution function (9). In this study, the model proposed by Guo et al. [19] is used to impose the pressure gradient.

As shown above, the computation of the fluid flow through a porous medium with the LBM is quite simple and very suited to parallel computing. Indeed, the collision step (12) and the full way bounce back scheme (14) are independently performed at each fluid node; and the streaming step (13) is performed from each fluid node to its neighboring fluid nodes. However, it consumes an important amount of memory as at least $(N+1)$ distribution functions f_i need to be stored at each node in addition to the macroscopic variables such as velocity $\boldsymbol{v}$ and density ρ. In this study, we use the open-source Palabos solver [29] to perform simulations. It is worth mentioning that all LBM simulations are performed in lattice units ($h^{lb} = 1$, $\Delta t^{lb} = 1$). A conversion from LBM quantities denoted with a superscript lb to those in the corresponding physical problem is performed as follows:

$$v = \frac{h}{\Delta t} v^{lb}, \quad \nu = \frac{h^2}{\Delta t} \nu^{lb}, \quad \nabla P = \frac{\rho}{\rho^{lb}} \frac{h}{\Delta t^2} \nabla P^{lb}, \quad K = h^2 K^{lb}. \tag{15}$$

3.3 FFT-based upscaling method

The FFT-based upscaling method presented in [7] relies on an extension of the homogenization problem (3) to the solid phase to benefit from an elementary solution, the Green function. In the extended problem, the whole domain Ω is assumed to be filled with a Newtonian fluid of uniform dynamic viscosity μ,

as in immersed boundary methods [26,31]:

$$\begin{aligned} &\nabla \cdot \boldsymbol{\sigma}' + \boldsymbol{f} = 0 && \text{in } \Omega \\ &\boldsymbol{\sigma}' = -p'\mathbf{1} + 2\mu\nabla^s \boldsymbol{v}' && \text{in } \Omega \\ &\nabla \cdot \boldsymbol{v}' = 0 && \text{in } \Omega \\ &\boldsymbol{v}' \text{ and } p' \text{ periodic} && \text{on } \partial\Omega \end{aligned} \tag{16}$$

The actual solid phase and the no-slip condition are indirectly accounted for by an appropriate choice of body force field $\boldsymbol{f}$ applied to the fluid[3].

The restriction to the solid-fluid interface Γ of the body force field $\boldsymbol{f}$ which allows us to retrieve the solution to the initial problem (3) from the extended problem (16) is the Lagrange multiplier of the no-slip boundary condition. Formally, this solution body force field is [8]:

$$\boldsymbol{f}_{\text{solution}} = -\boldsymbol{F} I_{\text{f}} - \boldsymbol{\sigma}_{|\text{f}} \cdot \nabla I_{\text{f}} \tag{17}$$

where $\boldsymbol{\sigma}_{|\text{f}}$ is the stress fluctuation solution to (3) evaluated on the fluid side of the interface Γ and I_{f} is the indicator function of the fluid phase, equal to 1 in Ω_{f} and 0 in Ω_{s}. The field (17) is understood in the sense of distributions: it features a surface distribution on Γ since $\nabla I_{\text{f}} = \delta_\Gamma \boldsymbol{n}_{\text{sf}}$ where δ_Γ is the Dirac surface distribution of Γ and $\boldsymbol{n}_{\text{sf}}$ the unit normal to Γ oriented from the solid to the fluid.

The extended problem (16) is of prime interest since the velocity field solution to (16) is formally known as:

$$\boldsymbol{v}'(\boldsymbol{x}) = \boldsymbol{V}' + \int_\Omega \boldsymbol{G}(\boldsymbol{x}-\boldsymbol{y}) \cdot \boldsymbol{f}(\boldsymbol{y}) \, \mathrm{d}V_y = \boldsymbol{V}' + (\boldsymbol{G} * \boldsymbol{f})(\boldsymbol{x}) \tag{18}$$

where $\boldsymbol{G}$ is by definition the Green function of the incompressible fluid of viscosity μ on the domain Ω with periodic boundary conditions and $\boldsymbol{V}'$ is an arbitrary constant which corresponds to the average velocity, that is $\overline{\boldsymbol{v}'}^{\Omega} = \boldsymbol{V}'$. The Green function $\boldsymbol{G}$ with periodic boundary conditions is known at a frequency $\boldsymbol{q}$ in the Fourier domain as [7]:

$$\hat{\boldsymbol{G}}(\boldsymbol{q}) = \begin{cases} \dfrac{1}{\mu \|\boldsymbol{q}\|^2} \left(\mathbf{1} - \dfrac{\boldsymbol{q} \otimes \boldsymbol{q}}{\|\boldsymbol{q}\|^2} \right) & \text{if } \boldsymbol{q} \neq \mathbf{0} \\ \mathbf{0} & \text{if } \boldsymbol{q} = \mathbf{0} \end{cases} \tag{19}$$

The convolution product in (18) can be readily evaluated by Fourier transforms and usual products in the Fourier space.

The velocity field solution to the homogenization problem (3) can then be obtained from the combination of (16) with (17), and by selecting $\boldsymbol{V}'$ to ensure $\boldsymbol{v}' = 0$ in Ω_{s}. Of course, since the stress fluctuation $\boldsymbol{\sigma}$ in (17) is not known unless the homogenization problem (3) is solved, this does not yet result in a practical method to solve the homogenization problem. Alternatively, one

[3] The bold letter $\boldsymbol{f}$ denotes a body force in this section, and must not be confused with the letter f which denotes the distribution function in the LBM method.

may construct upper bounds on the permeability from trial force fields which belong to the following set $\mathcal{F}(\boldsymbol{F})$ of admissible force fields:

$$\mathcal{F}(\boldsymbol{F}) = \left\{ \boldsymbol{f} \,\middle|\, \boldsymbol{f}(\boldsymbol{x}) = -\boldsymbol{F} \text{ if } \boldsymbol{x} \in \Omega_{\mathrm{f}} \,,\ \overline{\boldsymbol{f}}^{\Omega} = \boldsymbol{0} \right\} \,, \tag{20}$$

The first condition in (20) comes from the forcing term $\boldsymbol{F}$ which appears in problem (3) and the second one from the overall momentum balance of the RVE. From a stress energy theorem, one may prove [6]:

$$\boldsymbol{F} \cdot \boldsymbol{K} \cdot \boldsymbol{F} = \inf_{\boldsymbol{f} \in \mathcal{F}(\boldsymbol{F})} \mu \, \overline{\boldsymbol{f} \cdot \boldsymbol{G} * \boldsymbol{f}}^{\Omega} \tag{21}$$

The inf in (21) is met for the solution force (17) with a surface distribution, which hints that good trial force fields must be zero inside the solid and singular across the solid-fluid interface.

The FFT-based numerical method of [7] discretizes the extended problem (16) on a uniform grid as in Figure 2(c). The idea is to build an admissible discrete body force field $\boldsymbol{f} \in \mathcal{F}(\boldsymbol{F})$ and to minimize the energy in (21). On the grid, the index $\boldsymbol{n}$ is used to number the cells. Two sets of cells are defined (see Figure 2(c)):

- $\mathcal{C}_{\mathrm{f}}$ the set of fluid cells, comprising $\mathcal{N}_{\mathrm{f}}$ fluid cells ;
- $\mathcal{C}_{\mathrm{i}}$ the set of interface cells, comprising $\mathcal{N}_{\mathrm{i}}$ interface cells

Trial force fields $\boldsymbol{f} \in \mathcal{F}(\boldsymbol{F})$ are constructed as cell-wise constant fields, whose values $\boldsymbol{f}_{\boldsymbol{n}}$ on a cell $\boldsymbol{n}$ are $\boldsymbol{f}_{\boldsymbol{n}} = \boldsymbol{f}^{\boldsymbol{F}}_{\boldsymbol{n}} + \boldsymbol{f}^{\boldsymbol{\lambda}}_{\boldsymbol{n}}$ with:

$$\boldsymbol{f}^{\boldsymbol{F}}_{\boldsymbol{n}} = \begin{cases} -\boldsymbol{F} & \text{if } \boldsymbol{n} \in \mathcal{C}_{\mathrm{f}} \\ \dfrac{\mathcal{N}_{\mathrm{f}}}{\mathcal{N}_{\mathrm{i}}} \boldsymbol{F} & \text{if } \boldsymbol{n} \in \mathcal{C}_{\mathrm{i}} \\ 0 & \text{otherwise} \end{cases} \quad \text{and} \quad \boldsymbol{f}^{\boldsymbol{\lambda}}_{\boldsymbol{n}} = \begin{cases} 0 & \text{if } \boldsymbol{n} \in \mathcal{C}_{\mathrm{f}} \\ \boldsymbol{\lambda}_{\boldsymbol{n}} - \overline{\boldsymbol{\lambda}}^{\mathcal{C}_{\mathrm{i}}} & \text{if } \boldsymbol{n} \in \mathcal{C}_{\mathrm{i}} \\ 0 & \text{otherwise} \end{cases} \tag{22}$$

where $\overline{\boldsymbol{\lambda}}^{\mathcal{C}_{\mathrm{i}}}$ denotes the average over interface cells of the discrete field of unknowns $\boldsymbol{\lambda}$, computed as:

$$\overline{\boldsymbol{\lambda}}^{\mathcal{C}_{\mathrm{i}}} := \frac{1}{\mathcal{N}_{\mathrm{i}}} \sum_{\boldsymbol{n} \in \mathcal{C}_{\mathrm{i}}} \boldsymbol{\lambda}_{\boldsymbol{n}} \tag{23}$$

By construction, $\boldsymbol{f}^{\boldsymbol{F}} \in \mathcal{F}(\boldsymbol{F})$ and $\boldsymbol{f}^{\boldsymbol{\lambda}} \in \mathcal{F}(0)$ for any choice of the values $(\boldsymbol{\lambda}_{\boldsymbol{n}})_{\boldsymbol{n} \in \mathcal{C}_{\mathrm{i}}}$, hence $\boldsymbol{f} \in \mathcal{F}(\boldsymbol{F})$. The $\mathcal{N}_{\mathrm{i}}$ unknown vectors $(\boldsymbol{\lambda}_{\boldsymbol{n}})_{\boldsymbol{n} \in \mathcal{C}_{\mathrm{i}}}$ are determined by minimizing (21), which leads to the linear system of equations:

$$\forall \boldsymbol{n} \in \mathcal{C}_{\mathrm{i}} \,; \quad (\boldsymbol{G} * \boldsymbol{f})_{\boldsymbol{n}} - \overline{\boldsymbol{G} * \boldsymbol{f}}^{\mathcal{C}_{\mathrm{i}}} = 0 \tag{24}$$

Physically, (18) indicates that (24) amounts to meet the no-slip boundary condition $\boldsymbol{v}' = 0$ in a weak form over interface cells for the choice of the constant $\boldsymbol{V}' = -\overline{\boldsymbol{G} * \boldsymbol{f}}^{\mathcal{C}_{\mathrm{i}}}$. The system (24) can be split in a classical form with unknowns $(\boldsymbol{\lambda}_{\boldsymbol{n}})_{\boldsymbol{n} \in \mathcal{C}_{\mathrm{i}}}$ on the l.h.s. and the loading parameter $\boldsymbol{F}$ on the r.h.s. as:

$$\forall \boldsymbol{n} \in \mathcal{C}_{\mathrm{i}} \,; \quad (\boldsymbol{G} * \boldsymbol{f}^{\boldsymbol{\lambda}})_{\boldsymbol{n}} - \overline{\boldsymbol{G} * \boldsymbol{f}^{\boldsymbol{\lambda}}}^{\mathcal{C}_{\mathrm{i}}} = -(\boldsymbol{G} * \boldsymbol{f}^{\boldsymbol{F}})_{\boldsymbol{n}} + \overline{\boldsymbol{G} * \boldsymbol{f}^{\boldsymbol{F}}}^{\mathcal{C}_{\mathrm{i}}} \tag{25}$$

The linear operator which computes the l.h.s. in (25) from the unknowns $(\boldsymbol{\lambda_n})_{\boldsymbol{n}\in\mathcal{C}_\mathrm{i}}$ corresponds to a symmetric, semi-definite positive quadratic form from (21). The system can thus be solved using classical iterative solvers such as conjugate gradient or MINRES. The efficiency of the method partly comes from the fact that the matrix $[A]$ underlying the linear operator is not explicitly written nor stored: only the result of its action on a vector $\{X\} = (\boldsymbol{\lambda_n})_{\boldsymbol{n}\in\mathcal{C}_\mathrm{i}}$ of unknowns is required. This operation is sketched in Algorithm 1. Further, unknowns are defined only on interface voxels, which drastically reduces the memory footprint.

Algorithm 1 Operation of matrix $[A]$ on a vector $\{X\}$ in the l.h.s. of (25)

Input: $\{X\} = (\boldsymbol{\lambda_n})_{\boldsymbol{n}\in\mathcal{C}_\mathrm{i}}$
Output: $\{Y\} = [A]\cdot\{X\}$
1: **for all** voxels $\boldsymbol{n}$ **do** // **1.** map on grid
2: $F[\boldsymbol{n}] \leftarrow X[map(n)]$ **if** $\boldsymbol{n}\in\mathcal{C}_\mathrm{i}$ **else** 0
3: **end for**
4: $\hat{F} \leftarrow$FFT(F) // **2.** discrete Fourier transform
5: **for all** frequencies $\boldsymbol{k}$ **do** // **3.** apply Green function
6: $\hat{U}[\boldsymbol{k}] \leftarrow \hat{G}[\boldsymbol{k}]\cdot\hat{F}[\boldsymbol{k}]$
7: **end for**
8: $U \leftarrow$FFT$^{-1}(U)$ // **4.** inverse discrete Fourier transform
9: **for all** voxels $\boldsymbol{n}\in\mathcal{C}_\mathrm{i}$ **do** // **5.** reverse map from grid
10: $Y[map(\boldsymbol{n})] \leftarrow U[\boldsymbol{n}]$
11: **end for**
12: $\{Y\} \leftarrow \{Y\} - \mathrm{average}(\{Y\})$ // **6.** remove average

In Algorithm 1, a discretized Green function $\hat{\boldsymbol{G}}_{\boldsymbol{k}}$ is applied at step **3.** at each discrete frequency associated to the index $\boldsymbol{k}$ used to number the discrete frequencies in the Fourier space. Several types of discretization of the Green function are possible, as detailed in [7]. In this study, we always use the energy consistent discretization along with a force placement at the center of the cells ("consistent@center" scheme presented in [7]), since it provides the best accuracy for the microstructures under study. The right-hand side in (25) is computed by first creating the field $-\boldsymbol{f}^{\boldsymbol{F}}_{\boldsymbol{n}}$ on the discrete grid as detailed in (22), and second applying steps **2.** to **6.** of Algorithm 1.

The discrete force field (22) solution to system (25) is finally used in a discrete version of (18) to determine the solution velocity field. In practice, the convolution products in (25) are evaluated in the Fourier space from the Discrete Fourier Transform of the discrete fields (22), which is efficiently done by the FFT algorithm by steps **2.** to **4.** of Algorithm 1. Additional details regarding the FFT-based method can be found in [7].

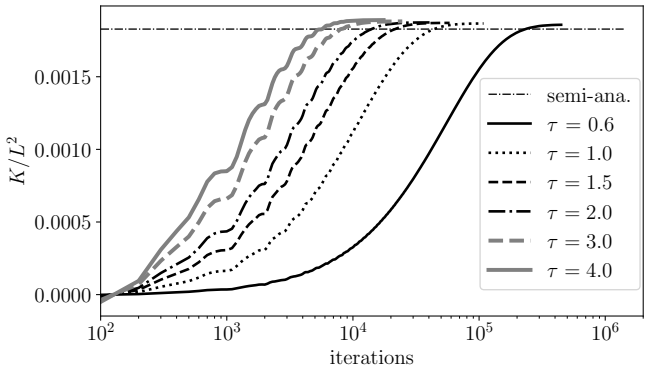

Fig. 4 Convergence of the permeability given by the LBM versus the number of iterations for different values of the relation time τ, in comparison with the semi-analytical solution.

4 Benchmark problems

4.1 2D square and circle inclusions

Let us study first the convergence of the LBM and FFT methods for two 2D benchmark cases where a solid square and a solid circle are centered at a square fluid area of length L, respectively. The square inclusion has a length $D = 0.5L$ and the circle inclusion has a diameter $D = 0.8L$. For the circle inclusion case, the semi-analytical solution of the permeability is $K/L^2 = 1.8280941789\times10^{-3}$ [7,37]. It should be noted that the uniform grid used for the discretization presented in Section 3.1 allows us to fully capture the geometry of the square even at low resolutions, while the geometry of the circle can be only well captured at sufficiently high resolution.

The LBM method presented in Section 3.2 is a dynamic method for which the flow velocities at the nodes, which are initially set to zero, evolve with time until reaching the final values at the quasi-static regime. This quasi-static regime is obtained by performing iterations until the coefficient of variation of the permeability K computed over 1000 iterations is smaller than 10^{-6}. The relaxation time τ used by the LBM must be carefully chosen as it controls the numerical stability and accuracy. Equation (11) implies that $\tau > 0.5$; nevertheless, there is no upper bound for τ. Figure 4 shows the convergence of the permeability K computed for the circle inclusion case versus the number of iterations for different values of τ. It can be seen that the higher the value of τ is, the faster the convergence is. However, the error in comparison with the semi-analytical value increases with an increase in τ. The value $\tau = 1$ appears to be a good compromise between the convergence rate and the error; furthermore, this value has been widely chosen in the literature. In the following, $\tau = 1$ is used for all the simulations performed with the LBM.

Figure 5 shows the relative error of the computed permeability K versus the resolution h/D for the square and circle inclusion cases, where h is the

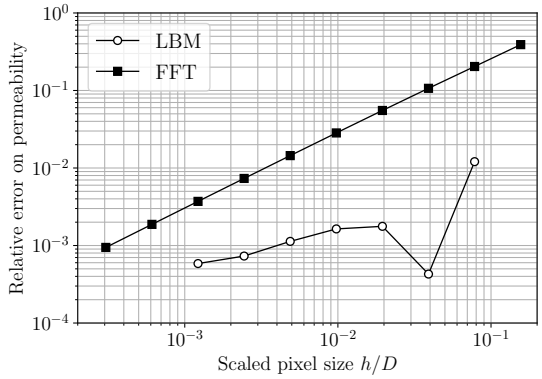

(a) Square

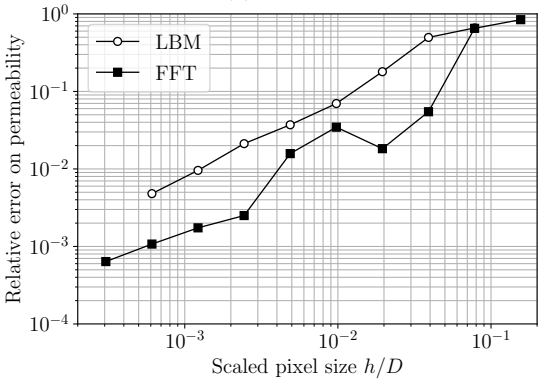

(b) Disk

Fig. 5 Relative error of the computed permeability versus the resolution h/D for the square and circle test cases

grid spacing. For the square case, there is no analytic or semi-analytic solution; nevertheless, as the convergence of K computed with the FFT method is linear with respect to the resolution h/D (see Figure 5.a), the exact solution when $h/D \to 0$ can be obtained by a linear extrapolation. It can be seen that, for the same resolution, the LBM method gives a higher accuracy on the computed permeability K than the FFT method for the square case but a lower accuracy for the circle case (see also [7] for a comparison of the variants of the FFT method on these examples). To analyze in further details the error made by the two methods, we compute the error of the velocity v_x given by each method at the center of each pixel for the circle case with this respect to the value given by the semi-analytical approach [37]. This error is normalized by the macroscopic velocity V_x computed with (5). For the LBM method, the velocity at the center of each pixel is computed as the average value of those at its four nodes. Figure 6 shows the error maps of v_x/V_x made by the two methods with a discretization of 64×64 pixels. It can be seen that the no-slip condition is not exactly imposed at the actual solid boundary by both methods. The LBM

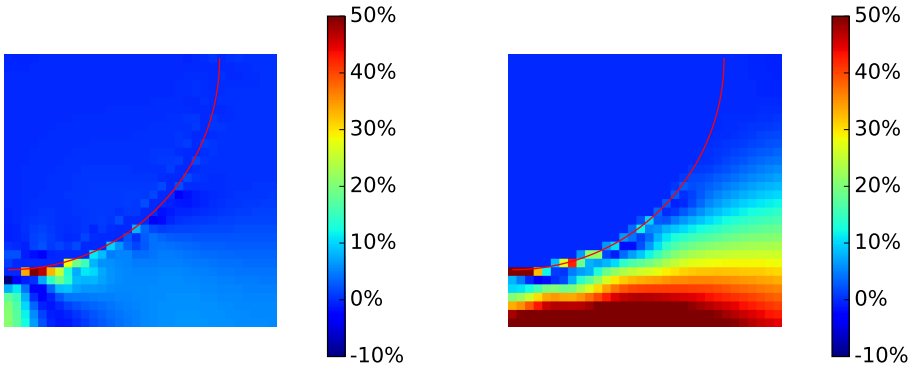

(a) FFT (b) LBM

Fig. 6 Error maps of v_x/V_x in the circle test case with a discretization of 64 × 64 pixels for (a) FFT method and (b) LBM method.

makes significantly larger errors far away from the boundary than the FFT method, which explains why the permeability K computed with the latter method is more accurate than the value given by the LBM in that case.

4.2 3D face centered cubic configuration

Let us now consider a 3D case of a face centered cubic (FCC) array of spheres of equal diameter D as shown in Figure 7 with the solid volume fraction being varied from 0.343 to 0.7405 (the densest packing). For this case, a semi-analytical solution for the permeability K has been established by Zick and Homsy [45] for different solid fractions. Figure 8 shows the scaled permeability K/D^2 computed with the LBM and FFT methods versus the solid fraction for a medium resolution $h/D = 0.0625$ ($D/h = 16$). The computed values of K/D^2 for a given solid fraction are compared to the semi-analytical value. It can be seen that both methods with the considered medium resolution give numerical values quite close to semi-analytical values. As a comparison, another fluid flow simulation method, called IBM (immersed boundary method) has been used by Knight et al. [26] for the same FCC case. The IBM and FFT methods share some common points: (i) they both extend the constitutive equations for the fluid (Navier-Stokes equations for the IBM and Stokes equations for the FFT) to the solid particles by introducing a source term representing the fluid-particle interaction force, (ii) the no-slip boundary conditions are imposed by choosing an appropriate source term, (iii) the constitutive equations are solved on a uniform grid. Unlike the FFT method, the IBM constructs the source term at some points inserted exactly at the boundary of the particles; therefore, the precise geometry of the particles is required by this method. Despite this additional computation effort, the permeability given by the IBM with the same resolution was found to be very different from the semi-analytical value

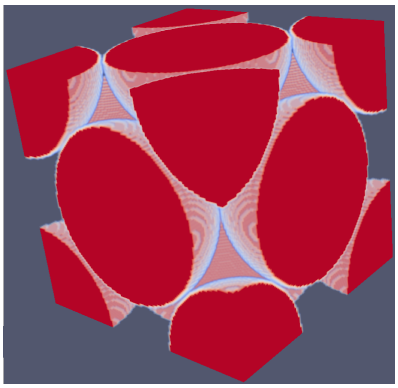

Fig. 7 A discretization of a face centered cubic periodic array of spheres with maximum solid fraction 0.7405.

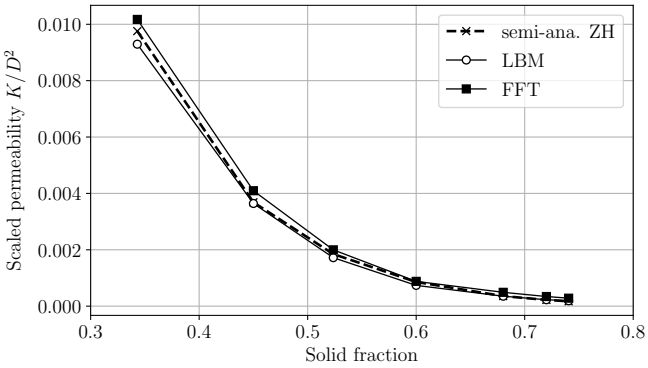

Fig. 8 Permeability K/D^2 given by the LBM and FFT methods versus the solid fraction for the 3D face centered cubic example with a resolution $h/D = 0.0625$ in comparison with the semi-analytical solution of Zick and Homsy.

given by Zick and Homsy (see Figure 3 in [26] for the drag coefficient which is inversely proportional to the permeability K). This difference remains quite large for a much better resolution $D/h = 64$. This allows us to conclude that the FFT and LBM methods give more accurate numerical results in terms of permeability than the IBM method used in [26].

Figure 9 shows the relative error of the numerical permeabilities K computed with the LBM and FFT methods versus the resolution h/D for the FCC case with the highest solid fraction 0.7405. The semi-analytical value $K/D^2 = 3.45 \pm 0.04 \times 10^{-4}$ obtained by Zick and Homsy [45] is chosen as the reference value. It can be seen that both methods reach relative errors within the accuracy of the reference solution, with more or less the same convergence of the computed permeability with respect to the resolution for this FCC case.

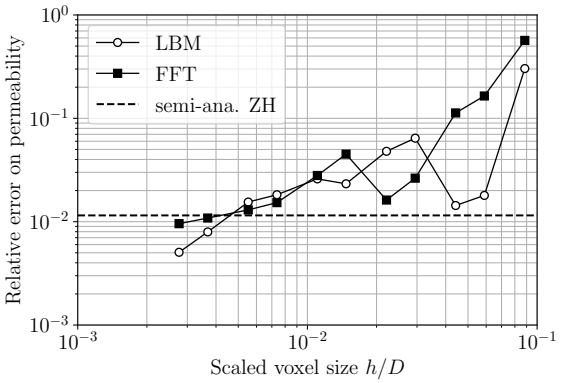

Fig. 9 Relative error on the computed permeability versus the resolution h/D for the face centered cubic case with the highest solid fraction 0.7405 with respect to the reference value $K/D^2 = 3.45 \pm 0.04 \times 10^{-4}$.

4.3 3D random samples of spheres

One monosized sample (UG1) with 512 balls and three uniformly graded samples (UG5, UG10 and UG15) with 512, 1728 and 4096 balls, respectively, are studied in this section. The porosity is controlled to be equal to around 0.38 for the four samples. We analyze here the effect of the discretization resolution on the computed permeability; the effect of the sample size will be analyzed in Section 5. For each sample, the grid spacing h and the computed permeability K are scaled by D_{50} and D_{50}^2, respectively (D_{50} is the particle diameter for which 50% of the particles by mass is finer).

Figure 10 shows the scaled permeability K/D_{50}^2 computed with the LBM and FFT methods versus the resolution h/D_{50} for the four samples UG1, UG5, UG10 and UG15. It can be seen that the permeabilities computed with the two methods converge differently with respect to the resolution but they both converge to almost the same value when h/D_{50} tends to 0. The FFT method exhibits a linear convergence when the resolution is sufficiently fine, allowing us to determine the limit of K/D_{50}^2 when $h/D_{50} \to 0$ by a linear extrapolation as shown in Figure 10. These linear convergence and extrapolation procedure are similar to those for numerical simulations using the finite-difference method used in [33]. The LBM has a non-monotonous convergence w.r.t. h/D_{50}, which gives more accurate results than the FFT method for the coarsest discretizations.

For the UG1 sample, the values of K/D_{50}^2 computed with the LBM and FFT methods converge actually toward 7.4×10^{-4} and 7.5×10^{-4}, respectively. In fact, this sample is a simulation of the monosized samples of glass beads which have been tested by Verneuil et al. [42]. The authors found a scaled permeability $K/D_{50}^2 = (6.1 \pm 0.7) \times 10^{-4}$ for these samples of glass beads with almost the same porosity, about 0.38, as that of the numerical sample UG1. Beavers et al. [4] also found a scaled permeability $K/D_{50}^2 = 6.3 \times 10^{-4}$ for

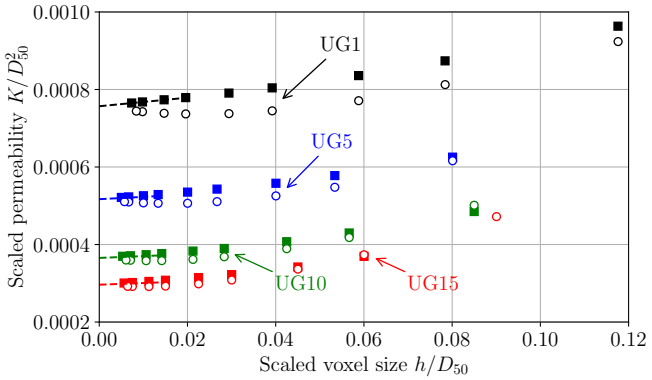

Fig. 10 Scaled permeability K/D_{50}^2 given by the LBM (○) and FFT (■) methods versus the resolution h/D_{50} for the UG1, UG5, UG10 and UG15 samples.

monosized samples of glass beads at a slightly lower porosity around 0.36. The computed values of K/D_{50}^2 computed with the LBM and FFT methods differ from the experimental mean values obtained by Verneuil et al. and Beavers et al. by about 21% and 17%, respectively. Moreover, when the porosity of this numerical sample is reduced to 0.36 which is the porosity of the samples tested by Beavers et al., the permeabilities K/D_{50}^2 given by both methods are about 6.2×10^{-4}, which is very close to the value obtained by Beavers et al. with a difference of only 2%. It is worth mentioning that the permeability is a parameter difficult to be precisely measured by experimental tests and the dispersion of obtained values is, in general, quite large. Indeed, in the experimental tests performed by Verneuil et al., the dispersion of obtained values of the permeability is about 12% with respect to the mean value. This comparison shows that the permeabilities computed with the LBM and FFT methods are in good agreement with the experimental values. One can also notice that the four numerical samples are at almost the same porosity but their scaled permeabilities K/D_{50}^2 are significantly different. This means that the permeability of granular soils depends strongly on the soil's GSD, which has been experimentally proved in the literature [23].

4.4 Computational efficiency of the LBM and FFT methods

Let us now discuss the efficiency of the LBM and FFT methods in terms of computational efforts and resources. As mentioned previously, the LBM is a dynamic method for which the numerical solution needs to be iterated until reaching the steady state. For the disk and square cases, the numbers of iterations for the LBM are quite large. For instance, with a resolution of 512 $\times$ 512 pixels, about 78 200 iterations are needed by the LBM for the circle case (see Figure 4). However, the number of iterations decreases greatly for the FCC case (about 10 800 iterations) and even more for the random samples

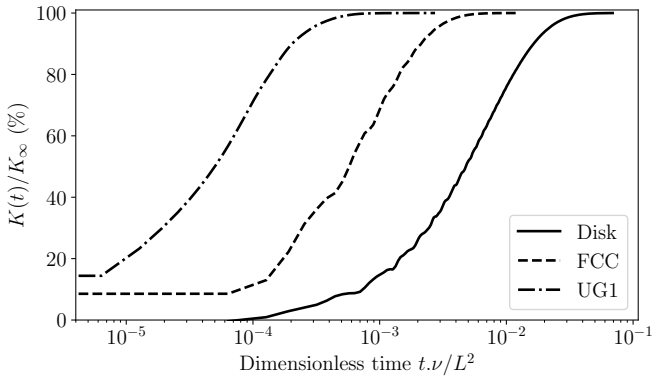

Fig. 11 The permeability K computed with the LBM, normalized by the value K_∞ at the steady state, versus the dimensionless time $t.\nu/L^2$ for the disk, FCC with the highest compacity and UG1 cases with a resolution $L/h = 512$.

(about 1 340 iterations for the UG1 sample) with the same resolution. It should be noted that the LBM introduces a perturbation to the system by applying a pressure gradient and the system will tend to the steady state after a characteristic time t^*. As a result, the iterations must be performed over this characteristic time t^* to get the value at the steady state. Figure 11 shows the evolution of the computed permeability K versus the dimensionless time $\tilde{t} = t.\nu/L^2$ (L is the size of the domain under consideration) for the disk, FCC with the highest compacity and UG1 cases with a resolution $L/h = 512$. In this figure, K is normalized by the value K_∞ at the steady state for each case. We can see that the dimensionless characteristic times $\tilde{t}^* = t^*.\nu/L^2$ are of order 10^{-2}, 10^{-3} and 10^{-4} for the disk, FCC and UG1 cases, respectively. It should be noted that the dimensionless time step $\Delta\tilde{t} = \Delta t.\nu/L^2$ used by the LBM is the same for all the three cases if the resolution is the same (see Equation (11)). As a result, the convergence is much faster for the UG1 case than for the disk case. The same conclusion was found when the disk is replaced by a sphere with the same size in 3D.

To explain why the dimensionless characteristic time $\tilde{t}^*$ for the UG1 case is smaller than that for the FCC case, which is, in turn, smaller than that for the disk case, we will compute the characteristic flow length L^* for each case. In fact, the characteristic time t^* for the viscous diffusion in a given porous medium is related to the characteristic flow length L^* by $t^* \propto (L^*)^2/\nu$. For a cylindrical channel, the characteristic length L^* is its diameter D. For granular media, the pore space is much more complex than a cylindrical channel. Such a pore space can be viewed as a set of many tortuous channels, each of which is composed of single pores and throats. Vincens et al. [43] define a single pore as the three-dimensional body of the relatively wide part of a channel that is constricted by two or more throats. The throats (or constrictions) are the narrowest cross-sections along any possible pathway. The characteristic flow length L^* is related to the distribution of the sizes of the throats, namely

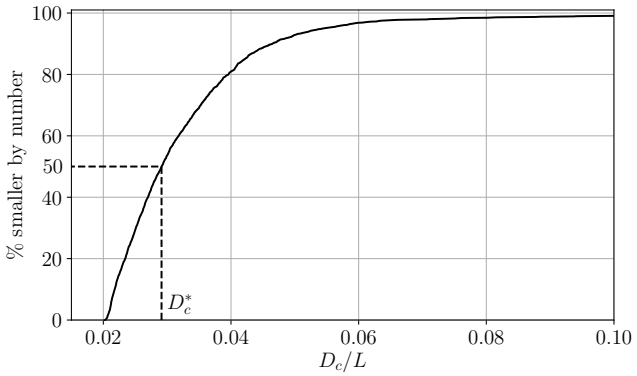

Fig. 12 Constriction size distribution (CSD) for the UG1 sample with 512 balls.

	Disk case	FCC case	UG1 sample
Characteristic flow length L^*/L (estimated)	0.2	0.109	0.029
Characteristic time $t^*\nu/L^2$ (estimated)	$\propto 0.04$	$\propto 0.012$	$\propto 0.00085$
Characteristic time $t^*\nu/L^2$ (LBM)	$\propto 10^{-2}$	$\propto 10^{-3}$	$\propto 10^{-4}$
Number of iterations (LBM)	78 200	10 800	1 340
Number of iterations (FFT)	100	200	220

Table 2 Estimated characteristic flow length L^* and time t^*, the value of the characteristic time t^* given by the LBM and the number of iterations used by the LBM and FFT methods for the disk, FCC and UG1 cases.

the constriction size distribution (CSD), of the porous medium under consideration. For the disk case, the sizes of the constrictions are $D_c^* = 0.2L$. For the FCC case with the highest compacity, the constrictions are composed of three spheres that touch each other. In this case, the sizes of the throats are $D_c^* = (\sqrt{1/3} - 1/2)4R \approx 0.109L$ ($R \approx 0.356L$). For the UG1 sample, we use the method developed by Nguyen et al. [34] to extract the sizes of the constrictions. Figure 12 shows the CSD of this sample, based on which the opening size D_c^* of the pore space can be estimated as the constriction diameter $D_{c,50}$ which corresponds to 50% smaller by number; accordingly, $D_c^* \approx 0.029L$ is found for the UG1 sample. This opening size D_c^* of the pore space is used for estimation of the characteristic flow length L^*. Table 2 shows the estimated characteristic flow length L^* and time t^*, the value of the characteristic time t^* given by the LBM and the number of iterations used by the LBM for the three considered cases. It can be seen that the characteristic flow length L^* of the UG1 sample is smaller than that of the FCC case which is, in turn, smaller than that of the disk case. Moreover, the order of magnitude of the estimated characteristic time t^* is quite consistent with that obtained with the LBM.

Unlike the LBM, the FFT method is a static one, and it needs to solve the linear system of equations (25) to obtain the force field $\boldsymbol{f}$ at the steady state. As mentioned in Section 3.3, this linear system of equations is solved in an iterative manner using the MINRES algorithm. Figure 13 shows the per-

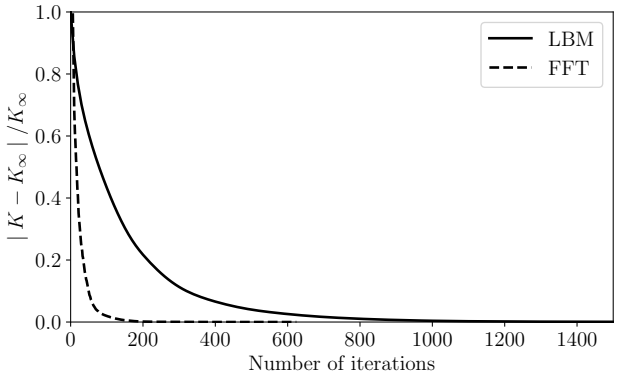

Fig. 13 Relative error between the permeability K computed at each iteration and the final value K_∞ versus the number of iterations for the LBM and FFT methods. The sample UG1 with 512 particles was used and the resolution $512 \times 512 \times 512$ was used for both methods.

meability K given by the LBM and FFT methods for the sample UG1 with a resolution $512 \times 512 \times 512$ voxels with respect to the number of iterations. The computed permeability K at each iteration is compared to the final value K_∞ obtained with each method. It can be seen that K computed with the FFT method converges much faster than that obtained with the LBM. Indeed, the FFT method needs only 220 iterations in comparison with 1 340 iterations for LBM to reach $|K - K_\infty|/K_\infty < 1\%$. For the disk inclusion and FCC cases, the number of iterations for the FFT method are very small in comparison with those for the LBM as can be seen in Table 2. It should be noted that the computation time depends not only on the number of iterations but also on the operations performed during each iteration. Therefore, to compare carefully the efficiency of these two methods, we run the code Palabos [29] for the LBM and the code developed by Bignonnet [7] for the FFT method on the same server Dell PowerEdge T640 for the UG1 case with the resolution $512 \times 512 \times 512$ voxels. Table 3 shows the computation time spent by these two methods for different numbers of threads used. For only one thread (the sequential computation), the FFT method is 3.9 times faster than the LBM. This ratio is 3.4 and 3.0 for the parallel computation with 10 and 20 threads, respectively. One can also remark that the scalability of the Palabos which is parallelized with Open MPI is slightly better than that of the FFT code which is parallelized with Open MP. Another advantage of the FFT method is that it requires much less memory to store information than the LBM which is well-known to be very memory intensive. Indeed, for the considered case, the memory consumed by the FFT method (about 5 GB) is 6 times smaller than the amount consumed by the LBM (about 30 GB). It is worth mentioning that a larger amount of memory requires a longer time for data transfer between the main memory source and the CPU memory. To conclude, on identical discretization grids, the FFT method prevails over the LBM method in terms of

Number of threads	Computation time	
	LBM	FFT
1	20 941 s	5 338 s
10	2 649 s	774 s
20	1 843 s	604 s

Table 3 Computation times for a UG1 sample with resolution 512^3: parallelization efficiency

efficiency to compute the permeability as it needs a much smaller number of iterations and a smaller amount of memory.

5 Determination of the grid resolution and sample size

5.1 Determination of the grid resolution

It is important to choose the voxel size h to obtain a reliable permeability K while keeping the computation time reasonable. Should the voxel size h be defined with respect to the maximum particle diameter D_{100}, the minimum diameter D_0, or another diameter D_X (D_X is the particle diameter at X % finer by mass)? To answer to this question, we plot the relative discretization error for the FFT and LBM methods versus the voxel size h normalized by a value D_X where X is varied from 0 to 100%. Figure 14 shows such a plot when D_{25} is chosen. To compute the relative discretization error, the reference value K_0 for both methods is determined by a linear extrapolation to $h = 0$ from the results obtained with the FFT method. We search for a value D_X such that the relative discretization errors at a given resolution h/D_X are close for the four different samples UG1, UG5, UG10 and UG15. The best candidate is D_{25} as shown in Figure 14, for which the error given by the FFT method scales linearly with h/D_{25} with a slope comprised between 1.15 and 1.46. This means that the voxel size h should be defined w.r.t. D_{25} rather than w.r.t. the minimum or maximum particle diameter. This figure shows clearly that the permeability K computed with the LBM converges better w.r.t. the voxel size than that computed with the FFT method at low and medium resolutions ($h/D_{25} \geq 0.04$). Nevertheless, at high resolution ($h/D_{25} < 0.04$), the convergence of the LBM becomes non-monotonous. To obtain a discretization error smaller than 5% w.r.t. the reference value K_0, the LBM requires a resolution $h/D_{25} \leq 6 \times 10^{-2}$, while the FFT method requires $h/D_{25} \leq 4 \times 10^{-2}$. This means that the resolution used for the FFT method should be about 1.5 times higher than that used by the LBM to achieve the same 5% accuracy. As shown in Table 3, the FFT method is almost 4 times faster than the LBM for the same resolution. Nevertheless, the computation time spent by the FFT method is increased by a factor of about 4.5 when the resolution is multiplied by a factor of 1.5. As a result, the computation times for both methods are comparable to achieve the same accuracy of the computed permeability. It is worth mentioning that these results are found for

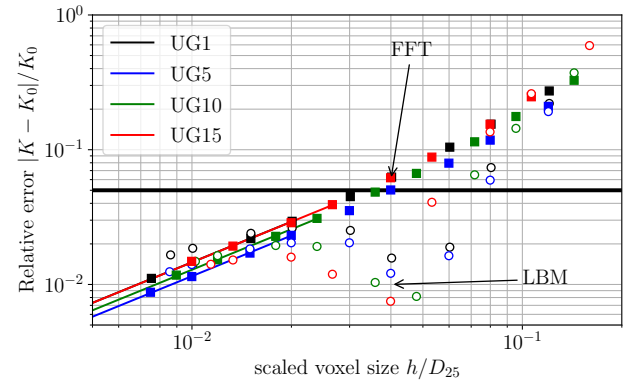

(a) absolute error (logscale)

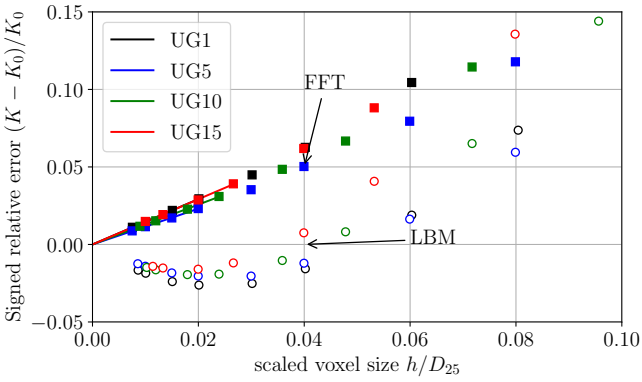

(b) signed error

Fig. 14 Discretization error for the LBM (○) and FFT (■) methods on uniformly graded samples as a function of the voxel size h. The reference permeability K_0 is computed by linear extrapolation to $h = 0$ from the results obtained with the FFT method. The horizontal thick line corresponds to 5% of discretization error.

the samples with linear gradation studied here, and they should be confirmed for other types of GSDs.

5.2 Definition and determination of the RVE size

5.2.1 Statistical definition of the RVE size

As simulations are performed on randomly generated samples of finite size, the issue of the representativity of the results must be addressed. By keeping constant all microstructure parameters such as the porosity and the grain size distribution, but randomizing the position of the grains, different realizations of the microstructure can be generated. The permeability K computed from a realization on a domain of finite volume $V = |\Omega|$ is thus a random variable

with some theoretical mean value of expectation $\mu_K(V) = E(K)$ and variance $\sigma_K^2(V) = E(K^2) - E(K)^2$ where $\sigma_K(V)$ is the standard deviation.

A first issue is that the average permeability $\mu_K(V)$ on realizations of finite volume V may contain a bias which depends on boundary conditions. A systematic bias on the homogenized stiffness or permeability arises with uniform Dirichlet or Neumann boundary conditions on finite samples [14,24], i.e. $\mu_K(V)$ decreases monotonously with V for Dirichlet boundary conditions, while it increases for Neumann ones. An analogue finite size effect arises when upscaling the stiffness in solid mechanics [24]. Unlike uniform Dirichlet or Neumann boundary conditions, Kanit et al. [24] showed that periodic boundary conditions as used here are unbiased even for finite sample size: the average property μ_K is almost independent on the size V of the sample provided that V is large enough to hold a few grains.

The second issue is the variability of the computed permeability, as quantified by the variance $\sigma_K^2(V)$. Intuitively, $\sigma_K^2(V)$ decreases with an increase in the domain size V for sufficiently large domains [11,24]. Two methods to estimate the variance $\sigma_K^2(V)$ w.r.t. V will be detailed in Sections 5.2.2 and 5.2.3.

The definition of the RVE then proceeds from the sampling theory of statistics. In the latter, the *population* average $\mu_K(V)$ and variance $\sigma_K^2(V)$ of the random variable K over all possible realizations are *a priori* unknown. They can be estimated by drawing randomly n realizations K_1, ..., K_n of the random variable K. The *empiric* estimators of the average $\overline{K}(V)$ and variance $S_K^2(V)$ computed from such random sampling, defined as $\overline{K}(V) = \frac{1}{n}\sum_{i=1}^{n} K_i$ and $S_K^2(V) = \frac{n}{n-1}(\overline{K^2} - \overline{K}^2)$ are also random variables, whose expectations are $E(\overline{K}(V)) = \mu_K(V)$ and $E(S_K^2(V)) = \sigma_K^2(V)$, respectively. Provided that n is large enough, the central limit theorem indicates that the random variable $\overline{K}$ follows a normal distribution with mean $\mu_K(V)$ and variance $\sigma_K^2(V)/n$. From the theory of estimation of statistics, a confidence interval $\mathcal{I} = [\overline{k} - \delta k; \overline{k} + \delta k]$ can then be constructed around an observation $\overline{k}$ of $\overline{K}(V)$ from a given drawing of n realizations such that the probability that $\mu_K(V) \in \mathcal{I}$ is equal to some level of confidence $1 - \alpha$ (e.g. $\alpha = 5\%$).

For example, assuming K is normally distributed, two cases can be faced:

1. If $\sigma_K^2(V)$ is known a priori (e.g. by a suitable model presented in Section 5.2.3): $\delta k = c\sigma_K(V)/\sqrt{n}$ where c is the $(1 - \alpha/2)$th percentile of the normal distribution, e.g. $c = 1.96$ for a level of confidence of 95% ($\alpha = 5\%$) as considered in Section 5.3. The relative error due to representativity issue is then defined as $\epsilon_K^{\text{rve}} = \delta k/\overline{k}$, that is:

$$\epsilon_K^{\text{rve}} = \frac{c\sigma_K(V)}{\overline{k}\sqrt{n}} \tag{26}$$

2. If $\sigma_K^2(V)$ is unknown and estimated by an observation $s_K(V)$ of $S_K(V)$: $\delta k = cs_K(V)/\sqrt{n}$ where c is the $(1 - \alpha/2)$th percentile of Student's t distribution with $n - 1$ degrees of freedom. One has e.g. $c = 2.09$ for $n = 20$ realizations and a level of confidence of 95% ($\alpha = 5\%$). The relative representativity error is obtained by replacing $\sigma_K(V)$ by $s_K(V)$ in (26).

Conversely, from the knowledge of the law of $S_K(V)$ w.r.t. V, one can define the RVE size as the volume V required to reach a target value of ϵ_K^{rve} by inversion of (26).

5.2.2 Estimation of the variance evolution by a direct method

In the seminal article of [24], the evolution law of the variance $S_K^2(V)$ w.r.t. V is determined from a series of simulations on domains of varying sizes. For each domain size V, a number n of realizations are drawn to compute an observation $s_K^2(V)$. Next, the evolution of the variance is modeled for sufficiently large domains by a power law as suggested by [11,24]:

$$\sigma_K^2(V) = \Sigma_K^2(0) \left(\frac{A_3^K}{V} \right)^{\lambda}, \qquad V \gg A_3^K \tag{27}$$

where λ is an exponent usually close to 1. In (27), $\Sigma_K^2(0)$ is the point variance of the velocity field in the direction of the applied pressure gradient $\boldsymbol{F}$. For example, if $\boldsymbol{F} = \boldsymbol{e}_x$, one has

$$\Sigma_K^2(0) = \overline{(v_x)^2}^{\Omega} - (\overline{v_x}^{\Omega})^2. \tag{28}$$

The quantity A_3^K is a characteristic volume of the fluctuation of the velocity field which generalizes the notion of integral range [24]. In practice, a fitting procedure directly provides λ and $\Sigma_K^2(0)(A_3^K)^{\lambda}$ and one does not need to compute separately $\Sigma_K^2(0)$ and A_3^K. We refer to this method as the direct method in what follows.

5.2.3 Estimation of the variance evolution by a filtering method

Instead of carrying out a great number of simulations required for the direct method, Abdallah et al. [1] suggested post-processing a single simulation on a large domain of size V. Estimates of the apparent permeability are computed by volume averaging of the velocity field on several disjoint subdomains of size $W < V$, for various sizes W. For each subdomain size W, an observation $s_K^2(W)$ of the variance of the apparent permeability is computed. One drawback is that as W increases, the number of disjoint subdomains that can be drawn from the large domain decreases. As a result, computed values of $s_K^2(W)$ are noisy for larger W; therefore, subdomains larger than $V/2^3$ cannot be investigated.

To overcome these limitations, Bignonnet [7] adapted this method by considering the subdomain as a sliding window. The idea is to compute the average of the velocity field in the neighborhood of *each* point $\boldsymbol{x}$ of the domain, the neighborhood being defined as a sliding window of size W centered at point $\boldsymbol{x}$. Then, for each domain size W, the variance of these averages are computed over all points. With this method, the subdomains used to compute the averages overlap. The main interest is that, for any size $W \leq V$, the number of subdomains is equal to the number of cells of the discretization, which is

large and then removes the noise. In practice, to compute the averages around each point, the method amounts to a filtering procedure. Let w be indicator function of a cube C_W of volume W centered at the origin, scaled such that $\overline{w}^{\Omega} = 1$. A filtered velocity field is computed by convolution as:

$$\boldsymbol{v}_w(\boldsymbol{x}) = \int_{\boldsymbol{y}\in\Omega} w(\boldsymbol{y})\boldsymbol{v}(\boldsymbol{x}-\boldsymbol{y})\,\mathrm{d}V_y = w*\boldsymbol{v} \quad \text{where} \quad w(\boldsymbol{x}) = \begin{cases} 1/W & \text{if } \boldsymbol{x} \in C_W \\ 0 & \text{else} \end{cases} \tag{29}$$

By construction, $\boldsymbol{v}_w(\boldsymbol{x})$ is the average of $\boldsymbol{v}$ over the cube of volume W centered at point $\boldsymbol{x}$. The convolution product in (29) is efficiently computed by FFT thanks to periodicity and use of a regular grid. As the filter volume W increases, the filtered field $\boldsymbol{v}_w$ becomes smoother. Ultimately as $W \to V$, $\boldsymbol{v}_w$ tends to a uniform velocity field equal to the macroscopic velocity $\boldsymbol{V}$. For a unit pressure gradient $\boldsymbol{F} = \boldsymbol{e}_x$ and each filter size W, the point variance of the filtered field is defined as:

$$\Sigma_K^2(W) = \overline{(v_x)_w^2}^{\Omega} - \left(\overline{(v_x)_w}^{\Omega}\right)^2 \tag{30}$$

Volume averages in (30) can be readily computed from voxel-wise values of $\boldsymbol{v}_w$. The point variance $\Sigma_K^2(W)$ quantifies the fluctuations of the filtered velocity field. It should be noted that, as $W \to 0$, $\Sigma_K^2(W)$ tends to the point variance of the non-filtered velocity field $\Sigma_K^2(0)$ defined in (28). Asymptotically as $A_3^K \ll W \ll V$, the dependence of $\Sigma_K^2(W)$ on W can be modeled as:

$$\Sigma_K^2(W) = \Sigma_K^2(0)\left[A_3^K\left(\frac{1}{W} - \frac{1}{V}\right)\right]^{\lambda}, \qquad A_3^K \ll W \ll V. \tag{31}$$

Expression (31) with $\lambda = 1$ has been derived for additive properties such as porosity [30] and has been used for the apparent permeability in [1] for a boolean model of monosized spheres or in [7] for a Voronoi mosaic model. We suggest here to adjust the value of the exponent λ like in (27), to obtain a better agreement to the data for polydisperse granular samples. In practice, the values of A_3^K and λ in (31) are fitted for filter volumes in the range $10A_3^K \leq W \leq 0.1V$, with a recursive evaluation of A_3^K. Once A_3^K and λ are determined by fitting (31), the variance $\sigma_K^2(V)$ of the permeability on a domain of size V, where V is the size of the simulation domain, is estimated by using (27) with the fitted values of A_3^K and λ.

5.3 Application to uniformly graded granular materials

A series of simulations is carried out using the FFT-based method for uniformly graded materials (see Figure 1) of the types UG1, UG5 and UG10. Samples are generated using the DEM with a porosity of $(37.8 \pm 0.2)\%$. The representativity issue is analyzed by carrying out $n = 20$ realizations of samples for each sample size. A coarse and a fine grid are used to compute the permeability of each sample. The voxel size h_{coarse} of the coarse grid (resp.

h_{fine}) is selected to reach a target discretization error of around 20% (resp. 6%) according to Figure 14. Table 4 shows the number of spheres and the grid sizes for each type of gradation.

	UG1	UG5	UG10
$D_{\max}/D_{\min}$	1.1	5	10
N_{spheres}	64, 216, 512, 1728, 4096, 13824	216, 512, 1728, 4096, 8000	1728, 4096, 8000, 13824
h_{coarse}/D_{25}	0.121	0.121	0.096
h_{fine}/D_{25}	0.046	0.046	0.037

Table 4 Numbers of spheres N_{spheres} and grid sizes h_{coarse} and h_{fine} used for each type of gradation.

The representativity error is studied by using the two methods introduced in Sections 5.2.2 and 5.2.3. For the direct method, the empiric estimations of the average permeability $\overline{K}(V)$ and the variance $\sigma_K^2(V)$ are computed from $n = 20$ realizations for each sample size and each type of gradation. Figure 15 shows the average permeability $\overline{K}(V)$ with respect to the sample size L_{RVE}/D_{25} for the three types of gradation. The relative error of $\overline{K}(V)$ is estimated using Student's t distribution with a confidence interval of 95% (case 2 presented in Section 5.2.1) and is represented by error bars in Figure 15. It can be seen that the average values $\overline{K}(V)$ of the permeability show no increasing nor decreasing trend as the sample size increases. Small fluctuations are visible since average values are computed over only $n = 20$ realizations, but these are of the same order of magnitude than the confidence intervals. This confirms that periodic boundary conditions are unbiased for the investigated sample sizes. A second observation is that the representativity errors decrease. Since the random variable $S_K^2(V)$ is an unbiased estimator of the variance $\sigma_K^2(V)$, a confidence interval on $\sigma_K^2(V)$ can be built around the observation $s_K^2(V)$ using a chi-square distribution. Estimated values of the variance $\sigma_K^2(V)$ with a confidence interval of 95% with respect to the number of spheres are displayed in Figure 17. Both fine and coarse grid resolutions are used to compute the permeability K and lead to similar values of the variance $\sigma_K^2(V)$.

For the filtering method, we first compute the point variance $\Sigma_K^2(W)$ of the filtered velocity with respect to the filter volume W for each independent realization. Figure 16 shows the results obtained for the samples UG5 with different sample sizes (20 independent realizations for each size). It can be seen that the curves of $\Sigma_K^2(W)$ for each sample size exhibit a large variability represented by lightly shaded areas. Next, the curve of $\Sigma_K^2(W)$ for each independent realization is fitted by the model (31) as illustrated in Figure 16. Finally, the fitted parameters A_3^K and λ are injected in (27) to estimate the variance $\sigma_K^2(V)$ where V is the volume of the sample obtained from the realization under consideration.

Figure 17 shows a comparison between values of the variance $\sigma_K^2(V)$ estimated by the direct method and by the filtering method for samples UG5

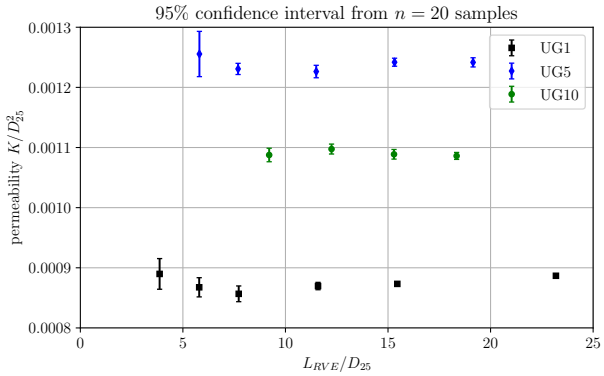

Fig. 15 Average permeability $\overline{K}(V)$ of uniformly graded materials with porosity 37.8±0.2% given by the direct method as a function of the RVE size. The error bars are estimated with 95% confidence intervals from Student's t distribution. Results are computed on the fine grid, with around 6% discretization error.

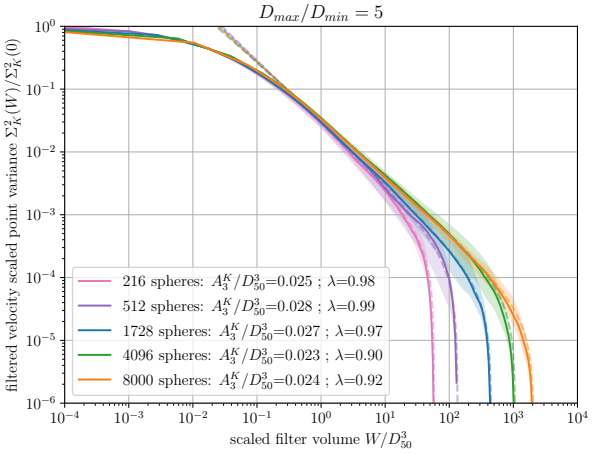

Fig. 16 Point variance $\Sigma_K^2(W)$ of the filtered velocity field versus the filter size W for the realizations of samples UG5 with different sizes. Lightly shaded areas: the range of variation among 20 realizations, full line: median curves, dotted line: fit of median curves by Equation (31).

with different sizes. It should be noted that, owing to the variability of the curves $\Sigma_K^2(W)$ shown in Figure 16, the estimated values of $\sigma_K^2(V)$ from the filtering method have themselves a quite large variability which is represented using distribution boxes in Figure 17. The estimated variances $\sigma_K^2(V)$ using both methods follow a quite similar trend, with differences being within the confidence intervals. That trend is fitted by using (27) from the median values given by the filtering method to obtain the variance $\sigma_K^2(V)$ w.r.t V. It is worth noting that the exponent λ in (31) fitted from a single realization in Figure 16 differs from the one in (27) fitted in Figure 17 on series of simulations of various sizes. Results similar to those shown in Figure 17 are obtained for the two

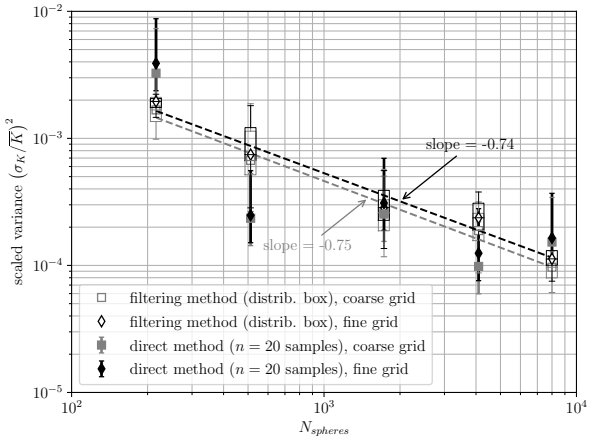

Fig. 17 Scaled variance of the permeability K versus the number of spheres, as required in Equation (26) to estimate representativity errors, for the simulations on samples UG5. Dotted lines: power-law fits of median values obtained with the filtering method. Error bars for the direct method are drawn from the 95% confidence interval on the variance from a chi-square estimator.

other types of gradation UG1 and UG10. The exponent λ in (27) is found to decrease with increasing ratio $D_{\max}/D_{\min}$ with values 0.99, 0.74 and 0.69 for samples UG1, UG5 and UG10, respectively.

The values of the variance σ_K^2 obtained from the direct method, the filtering method and the relation (27) with the parameters obtained from the aforementioned fitting method are injected in (26) to estimate the representativity error ϵ_K^{rve} for a given sample size. Figure 18 shows the representativity error ϵ_K^{rve} as a function of the sample size L_{RVE} normalized by the particle diameter D_{40} for the three types of gradation UG1, UG5 and UG10. The diameter D_{40} was chosen as it allows us to obtain close values of ϵ_K^{rve} for the three types of gradation at the same value of L_{RVE}/D_{40}. For the three types of gradation investigated here, the representativity error is found to be below 5% provided that the length of the domain is at least 7 times the diameter D_{40}.

6 Conclusions

In this paper, we present a comparison between the LBM and FFT based method used to compute the permeability K of granular assemblies. Different benchmark cases have been considered: 2D square and disk inclusions, 3D face centered cubic array (FCC) and 3D random uniformly graded samples. The DEM was used to simulate the latter granular samples which have periodic boundary conditions. We studied four linear gradations, UG1, UG5, UG10 and UG15 with $D_{\max}/D_{\min} = 1.1$, 5, 10 and 15, respectively.

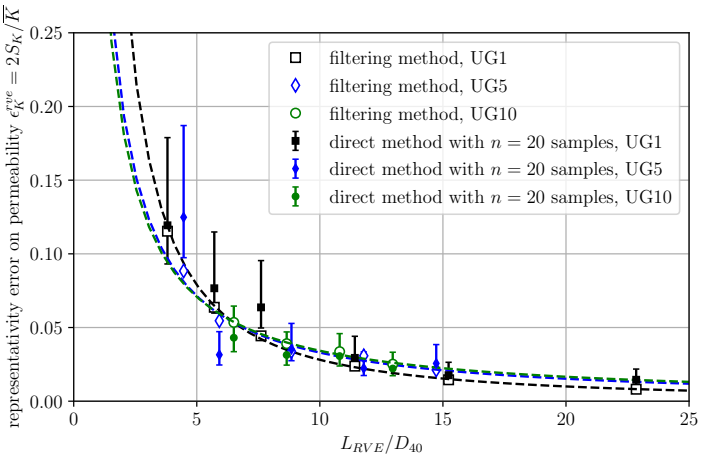

Fig. 18 Representativity error $\epsilon_K^{\mathrm{rve}}$ estimated with a 95% confidence interval by the direct and filtering methods for the three types of gradation, as a function of the sample size L_{RVE} scaled by the particle diameter D_{40}. Dotted lines: power-law fits of median values given by the filtering method.

For the square inclusion case, the permeability computed with the LBM is more accurate than that computed with the FFT method, while the inverse was found for the disk case. For the FCC case, both methods give almost the same accuracy in comparison with the semi-analytical values obtained by Zick and Homsy [45] for different solid fractions. For the sample UG1 which corresponds to glass beads, the values of K given by both methods are quite close to the experimental values obtained by Verneuil et al. [42] and Beavers et al. [4].

For the 3D random samples, the permeability K computed with the LBM converges better with respect to the discretization resolution (grid spacing h) than that computed with the FFT method for coarse to moderately fine discretization. In addition, the FFT method shows a linear convergence with respect to h when the latter is sufficiently fine, allowing us to extrapolate the value of K for $h = 0$. For all the four linear gradations mentioned above, the discretization error appears to be controlled by D_{25}, the 25% passing by mass grain diameter. To obtain relative discretization errors smaller than 5%, the FFT method and LBM requires $h/D_{25} \leq 4 \times 10^{-2}$ and 6×10^{-2}, respectively. In particular, for the FFT method, the relative discretization error is linear with h and lower than $1.5h/D_{25}$.

From a computational point of view, the FFT method is much more efficient than the LBM for the same discretization resolution as the former needs less iterations and consumes less memory than the latter. Nevertheless, as the convergence of the LBM with respect to the discretization resolution is better than that of the FFT method, the computational efficiencies of both methods are comparable to reach the same accuracy for the computed values of the permeability.

The RVE size is determined for a target variability of the permeability computed on finite sized samples of uniformly graded samples. The direct method involves many realizations of similar random samples, while the filtering method relies on a single sample, which is faster. Both methods have been shown to yield comparable estimates of the variability, within error bounds. They both exhibit very little sensitivity to the discretization grid, implying that rather coarse grids can be used to estimate the RVE size. Finally, it is shown that a Representative Volume Element (RVE) size larger than $7D_{40}$ guarantees a variability of the computed permeability below 5% for the uniformly graded samples UG1, UG5 and UG10 investigated here.

This work provides useful guidelines regarding the choice of a numerical method to compute the permeability of granular samples simulated with the DEM, its discretization errors and the representativity issues. It will serve as a basis to optimize future numerical works which aim at investigating the relationship between the porosity, the grain size distribution, the pore characteristics and the permeability for more realistic gradations.

Acknowledgements

This work was partly funded by the French National Research Agency under grant ANR-21-CE22-0005-01.

References

1. Abdallah, B., Willot, F., Jeulin, D.: Stokes flow through a boolean model of spheres: Representative volume element. Transport in Porous Media **109**(3), 711–726 (2015)
2. Auriault, J.L., Geindreau, C., Boutin, C.: Filtration law in porous media with poor separation of scales. Transport in Porous Media **60**(1), 89–108 (2005)
3. Auriault, J.L., Sanchez-Palencia, E.: Etude du comportement macroscopique d'un milieu poreux saturé déformable. Journal de Mécanique **16**, 575–603 (1977)
4. Beavers, G.S., Sparrow, E., Rodenz, D.: Influence of bed size on the flow characteristics and porosity of randomly packed beds of spheres. Journal of Applied Mechanics **40**(3), 655–660 (1973)
5. Bhathnagor, P., Gross, E., Krook, M.: A model for collision processes in gases. Physical Review **94**(3), 511 (1954)
6. Bignonnet, F.: Upper bounds on the permeability of random porous media. Transport in Porous Media **122**(1), 57–76 (2018)
7. Bignonnet, F.: Efficient FFT-based upscaling of the permeability of porous media discretized on uniform grids with estimation of RVE size. Computer Methods in Applied Mechanics and Engineering **369**, 113237 (2020)
8. Bignonnet, F.: Micromechanical schemes for Stokes to Darcy homogenization of permeability based on generalized Brinkman inhomogeneity problems. International Journal of Engineering Science **172**, 103622 (2022)
9. Bignonnet, F., Dormieux, L.: FFT-based bounds on the permeability of complex microstructures. International Journal for Numerical and Analytical Methods in Geomechanics **38**(16), 1707–1723 (2014)
10. Bouzidi, M., Firdaouss, M., Lallemand, P.: Momentum transfer of a Boltzmann-lattice fluid with boundaries. Physics of fluids **13**(11), 3452–3459 (2001)
11. Cailletaud, G., Jeulin, D., Rolland, P.: Size effect on elastic properties of random composites. Engineering computations **11**, 99–110 (1994)

12. Carman, P.C.: Fluid flow through granular beds. Chemical Engineering Research and Design **75**, S32–S48 (1997)
13. Coelho, D., Thovert, J.F., Adler, P.M.: Geometrical and transport properties of random packings of spheres and aspherical particles. Physical Review E **55**, 1959–1978 (1997)
14. Du, X., Ostoja-Starzewski, M.: On the size of representative volume element for Darcy law in random media. Proceedings of the Royal Society A **462**, 2949–2963 (2006)
15. Eichheimer, P., Thielmann, M., Fujita, W., Golabek, G.J., Nakamura, M., Okumura, S., Nakatani, T., Kottwitz, M.O.: Combined numerical and experimental study of microstructure and permeability in porous granular media. Solid Earth **11**(3), 1079–1095 (2020)
16. Ene, H., Sanchez-Palencia, E.: Equations et phénomènes de surface pour l'écoulement dans un modèle de milieu poreux. Journal de Mécanique pp. 73–108 (1975)
17. Fry, J.: Lessons on internal erosion in embankment dams from failures and physical models. In: Proceeding of 8th International Conference on Scour and Erosion (ICSE8), pp. 41–58 (2016)
18. Gueven, I., Frijters, S., Harting, J., Luding, S., Steeb, H.: Hydraulic properties of porous sintered glass bead systems. Granular Matter **19**(2), 1–21 (2017)
19. Guo, Z., Zheng, C., Shi, B.: Discrete lattice effects on the forcing term in the lattice Boltzmann method. Physical Review E **65**(4), 046308 (2002)
20. He, X., Luo, L.S.: Lattice Boltzmann model for the incompressible Navier–Stokes equation. Journal of statistical Physics **88**(3), 927–944 (1997)
21. He, X., Luo, L.S.: Theory of the lattice Boltzmann method: From the Boltzmann equation to the lattice Boltzmann equation. Physical review E **56**(6), 6811 (1997)
22. He, X., Zou, Q., Luo, L.S., Dembo, M.: Analytic solutions of simple flows and analysis of nonslip boundary conditions for the lattice Boltzmann BGK model. Journal of Statistical Physics **87**(1), 115–136 (1997)
23. Indraratna, B., Nguyen, V.T., Rujikiatkamjorn, C.: Hydraulic conductivity of saturated granular soils determined using a constriction-based technique. Canadian Geotechnical Journal **49**(5), 607–613 (2012)
24. Kanit, T., Forest, S., Galliet, I., Mounoury, V., Jeulin, D.: Determination of the size of the representative volume element for random composites: statistical and numerical approach. International Journal of solids and structures **40**(13-14), 3647–3679 (2003)
25. Kenney, T., Chahal, R., Chiu, E., Ofoegbu, G., Omange, G., Ume, C.: Controlling constriction sizes of granular filters. Canadian Geotechnical Journal **22**(1), 32–43 (1985)
26. Knight, C., O'Sullivan, C., van Wachem, B., Dini, D.: Computing drag and interactions between fluid and polydisperse particles in saturated granular materials. Computers and Geotechnics **117**, 103210 (2020)
27. Koltermann, C.E., Gorelick, S.M.: Fractional packing model for hydraulic conductivity derived from sediment mixtures. Water Resources Research **31**(12), 3283–3297 (1995)
28. Kuhn, M.R., Sun, W., Wang, Q.: Stress-induced anisotropy in granular materials: fabric, stiffness, and permeability. Acta Geotechnica **10**(4), 399–419 (2015)
29. Latt, J., Malaspinas, O., Kontaxakis, D., Parmigiani, A., Lagrava, D., Brogi, F., Belgacem, M.B., Thorimbert, Y., Leclaire, S., Li, S., et al.: Palabos: parallel lattice Boltzmann solver. Computers & Mathematics with Applications **81**, 334–350 (2021)
30. Matheron, G.: The theory of regionalized variables and its applications. Ecole Nationale Supérieure des Mines, Paris (1971)
31. Mittal, R., Iaccarino, G.: Immersed boundary methods. Annual Review of Fluid Mechanics **37**(1), 239–261 (2005)
32. Monchiet, V., Bonnet, G., Lauriat, G.: A FFT-based method to compute the permeability induced by a Stokes slip flow through a porous medium. Comptes Rendus de Mécanique **337**, 192–197 (2009)
33. Mourzenko, V., Thovert, J.F., Vizika, O., Adler, P.M.: Geometrical and transport properties of random packings of polydisperse spheres. Physical Review E **77**, 066306 (2008)
34. Nguyen, N.S., Taha, H., Marot, D.: A new Delaunay triangulation-based approach to characterize the pore network in granular materials. Acta Geotechnica pp. 1–19 (2021)
35. Odong, J.: Evaluation of empirical formulae for determination of hydraulic conductivity based on grain-size analysis. Journal of American Science **3**(3), 54–60 (2007)
36. O'Sullivan, C.: Particulate discrete element modelling: a geomechanics perspective. CRC Press (2011)

37. Sangani, A., Acrivos, A.: Slow flow past periodic arrays of cylinders with application to heat transfer. International Journal of Multiphase Flow **8**(3), 193–206 (1982)
38. Sanvitale, N., Zhao, B., Bowman, E., O'Sullivan, C.: Particle-scale observation of seepage flow in granular soils using PIV and CFD. Géotechnique pp. 1–18 (2021)
39. Sheikh, B., Pak, A.: Numerical investigation of the effects of porosity and tortuosity on soil permeability using coupled three-dimensional discrete-element method and lattice Boltzmann method. Physical Review E **91**(5), 053301 (2015)
40. Taha, H., Nguyen, N.S., Marot, D., Hijazi, A., Abou-Saleh, K.: Micro-scale investigation of the role of finer grains in the behavior of bidisperse granular materials. Granular Matter **21**(2), 28 (2019)
41. Tran, D.K., Prime, N., Froiio, F., Callari, C., Vincens, E.: Numerical modelling of backward front propagation in piping erosion by DEM-LBM coupling. European Journal of Environmental and Civil Engineering **21**(7-8), 960–987 (2017)
42. Verneuil, E., Durian, D.J.: Permeability of mixed soft and hard granular material: Hydrogels as drainage modifiers. The European Physical Journal E **34**(7), 1–7 (2011)
43. Vincens, E., Witt, K.J., Homberg, U.: Approaches to determine the constriction size distribution for understanding filtration phenomena in granular materials. Acta Geotechnica **10**(3), 291–303 (2015)
44. Šmilauer, V., et al.: Yade Documentation 2nd ed. The Yade Project (2015). DOI 10.5281/zenodo.34073. http://yade-dem.org/doc/
45. Zick, A., Homsy, G.: Stokes flow through periodic arrays of spheres. Journal of fluid mechanics **115**, 13–26 (1982)